small methods
www.small-methods.com

Anomalous Impact of Mechanochemical Treatment on the Na-ion Conductivity of Sodium Closo-Carbadodecaborate Probed by X-Ray Raman Scattering Spectroscopy

Valerio Gulino, Alessandro Longo,* Laura M. de Kort, Hendrik P. Rodenburg, Fabrizio Murgia, Matteo Brighi, Radovan Černý, Christoph J. Sahle, Martin Sundermann, Hlynur Gretarsson, Frank de Groot, and Peter Ngene**

Solid-state sodium ion conductors are crucial for the next generation of all-solid-state sodium batteries with high capacity, low cost, and improved safety. Sodium closo-carbadodecaborate ($NaCB_{11}H_{12}$) is an attractive Na-ion conductor owing to its high thermal, electrochemical, and interfacial stability. Mechanical milling has recently been shown to increase conductivity by five orders of magnitude at room temperature, making it appealing for application in all-solid-state sodium batteries. Intriguingly, milling longer than 2 h led to a significant decrease in conductivity. In this study, X-ray Raman scattering (XRS) spectroscopy is used to probe the origin of the anomalous impact of mechanical treatment on the ionic conductivity of $NaCB_{11}H_{12}$. The B, C, and Na K-edge XRS spectra are successfully measured for the first time, and ab initio calculations are employed to interpret the results. The experimental and computational results reveal that the decrease in ionic conductivity upon prolonged milling is due to the increased proximity of Na to the $CB_{11}H_{12}$ cage, caused by severe distortion of the long-range structure. Overall, this work demonstrates how the XRS technique, allowing investigation of low Z elements such as C and B in the bulk, can be used to acquire valuable information on the electronic structure of solid electrolytes and battery materials in general.

1. Introduction

In the development of more efficient energy storage systems, sodium-based all-solid-state batteries are a viable alternative to the current Li-ion technology. All-solid-state sodium batteries combine the advantages of all-solid-state lithium batteries, i.e., both intrinsically enhanced safety and extended temperature operating range, with a larger availability and lower cost of Na compared to Li.[1,2]

Solid-state electrolytes, i.e., ion conductors, are crucial for all-solid-state batteries, hence they have been the focus of several battery-related investigations in the last decades. Among all the classes of materials studied so far for this application, complex hydrides have gained particular attention as both Li and post-Li electrolytes.[3,4] Complex hydrides are solid materials with low density, low toxicity, and soft mechanical properties.[3–5] Especially as Na-ion conductors, hydroborates with large cluster

---

V. Gulino, L. M. de Kort, H. P. Rodenburg, F. de Groot, P. Ngene
Materials Chemistry and Catalysis
Debye Institute for Nanomaterials Science
Utrecht University
Utrecht 3584 CG, The Netherlands
E-mail: v.gulino@uu.nl; p.ngene@uu.nl

A. Longo, C. J. Sahle
European Synchrotron Radiation Facility
Grenoble F-38000, France
E-mail: alessandro.longo@esrf.fr

A. Longo
Istituto per lo Studio dei Materiali Nanostrutturati
Consiglio Nazionale delle Ricerche
Palermo 90146, Italy

F. Murgia, M. Brighi, R. Černý
Laboratory of Crystallography
Department of Quantum Matter Physics
University of Geneva
Geneva CH-1211, Switzerland

F. Murgia
Dipartimento di Scienze Chimiche
Fisiche
Matematiche e Naturali
Università degli Studi di Sassari
Sassari 07100, Italy

M. Sundermann, H. Gretarsson
Deutsches Elektronen-Synchrotron DESY
D-22607 Hamburg, Germany

M. Sundermann
Max Planck Institute for Chemical Physics of Solids
D-01187 Dresden, Germany

The ORCID identification number(s) for the author(s) of this article can be found under https://doi.org/10.1002/smtd.202300833

DOI: 10.1002/smtd.202300833

anions, $[B_xH_x]^{2-}$ ($x = 10, 12$), and their C-derivatives $[CB_{x-1}H_x]^-$ have shown properties such as: a) high oxidative stability[6–8] due to the strong electronic delocalization among their cages,[9,10] b) good compatibility with metallic Na,[11] c) high thermal stability,[9] and d) low area-specific resistance,[12] which are desirable electrolyte properties for next-generation all-solid-state batteries.[4,5]

In this sodium hydroborate system, the Na-ion mobility is strongly related to the physicochemical properties of the polyhedral anions, due to the strong correlation between the anion rotation rates and the cation diffusivity.[13–15] In addition, specifically in the carba-closo cages $[CB_{x-1}H_x]^-$, the larger size of C compared to B, as well as the higher acidity of the H bonded to it, compared to that of H in B-H bonds, results in a larger steric effect and lower electron density, respectively. These two effects enhance the cation repulsion thereby influencing the ionic conductivity.[13] In these compounds, fast Na^+ conductivity is achieved after an order-disorder phase transition above room temperature (RT). Lowering the transition temperature, i.e., destabilizing the anion sublattice and thereby enabling a fast anion rotation, can be induced using various strategies such as atom deficiency, e.g. increasing the Na defect concentrations,[16] anion substitution,[11,17,18] and composite formation.[19–21]

Mechanical milling is also a well-established technique to promote perturbation in solid crystals, i.e., stabilizing non-equilibrium phases in various materials, or accumulation of structural defects.[22] For instance, using molecular dynamics simulations, Dawson et al.[23] predicted that the ionic conductivity of LGPS can be increased by a factor of 3 if local disorder is introduced. Recently, it has been experimentally demonstrated that mechanical milling is able to suppress the order-disorder phase transition in $NaCB_{11}H_{12}$ (NCB).[24] NCB is stable at RT with an ordered orthorhombic ($Pca2_1$) structure that undergoes a polymorphic phase transition at ≈120 °C to a cubic (Fm-3m) structure.[25] Murgia et al.[24] reported the stabilization of the cubic body-centered (bcc) polymorph of NCB at RT via high-energy mechanical milling, after only 15 min. As expected, the Na-ion conductivity increased continuously with the milling time, reaching a maximum after 45 min, i.e., 4 mS cm^{-1} at RT. Unexpectedly, further mechanical grinding up to 2 h, provoked a decrease in conductivity, and prolonged milling to 6 h led to a profound decrease in the Na-ion conductivity (9.78×10^{-9} S cm^{-1} at RT) accompanied by a significant decrease in crystallinity. The initial increase in the Na-ion conductivity upon milling for 45 min was ascribed to the stabilization of the bcc polymorph at RT, a structure with a less efficient anion-packing compared to the orthorhombic starting structure, yet providing better and larger conduction pathways for Na^+ due to a shorter diffusion distance.[9,24] However, the reason for the reduced conductivity after milling times longer than 45 min has not been investigated in detail. It is well established that ball milling introduces defects that are deemed beneficial for ion conductivity in most solid electrolytes. To understand these anomalous effects in NCB, X-ray diffraction, IR and Raman spectroscopies have been used to characterize the samples milled longer than 4 h, but the information that could be extracted from these techniques was not sufficient to explain the drastic decrease in conductivity.

X-ray Raman Scattering (XRS),[26] is a technique in which the intensity of scattered photons is measured as a function of the energy loss between the incident and the scattered hard X-ray energy, revealing information similar to soft X-ray absorption spectra. The experimental advantages of hard X-ray techniques are retained, making XRS an ideal tool for obtaining chemical information on light elements with bulk sensitivity, even for nanocrystalline and amorphous samples contained in complicated sample environments.[27–31] In addition, it is possible to perform in-situ measurements,[27–29,32] as well as 3D tomography studies[33–35] by utilizing the chemical imaging properties of XRS.

In this work, we demonstrate, for the first time, the use of XRS to study the origin of such a change in the ionic conductivity of NCB upon milling. Firstly, by measuring the boron, carbon, and sodium K-edge of the $NaCB_{11}H_{12}$, and, secondly, by correlating the change in the electronic structure of the NCB to the ionic conductivity as a function of the milling time. By comparing ab initio calculated XRS spectra to the experimental ones, we conclude that the increased proximity of the Na^+ to the $CB_{11}H_{12}^-$, arising from severe structural distortion during prolonged mechanical milling, leads to the dramatic reduction in the Na-ion conductivity.(**Figure 1**)

2. Results

2.1. X-Ray Raman Scattering Spectra

The normalized and background subtracted B, C, and Na K-edges spectra obtained for the NCB milled at different times are shown in **Figure 2**. The B K-edge spectra (Figure 2a) show three characteristic features typical to boron compounds. The first peak ≈191 eV is attributed to the transition of a core B 1s electron from the carbo-closo anion $[CB_{11}H_{12}]^-$ to an unoccupied boron antibonding π^* ($2a_1$) orbital. We assign the second peak ≈196 eV to the transition of B 1s electrons to unoccupied σ^* orbitals of t_2 symmetry in the pentacoordinated B in the $CB_{11}H_{12}$ cage, as observed in $Li_2B_{12}H_{12}$, and tetragonally coordinated B compounds such as preobrazhenskite ($Mg_3B_{11}O_{15}(OH)_9$). Finally, the broad feature ≈200–204 eV is associated with the transition of a B 1s electron to an unoccupied σ^* with a_1 and t_2 symmetry,[36] as also observed in $LiBH_4$, $NaBH_4$, and $Li_2B_{12}H_{12}$. Similarly, the C K-edge (Figure 2b), shows three distinct peaks arising from excitations of the C 1s core electron to unoccupied π^* (≈288 eV) and σ^* (>290 eV) states. Specifically, the peak at 288 eV is due to a transition to the C $2p_z$ orbital, while the peaks at 292 and 297 eV are associated with a transition to C 2s, $2p_x$ and $2p_y$ orbitals.[37] In the Na K-edge, a pre-edge feature is present at ~1074 eV, which originates from a monopolar 1s → 3s transition. The peak at ~1078 eV is usually assigned to a Na 1s → 3p transition, while the less distinct (broad) band ≈1085 eV is attributed to multiple scattering events beyond the immediate environment of the Na.

From Figure 2, it can be seen that when the milling time is longer than 1 h distinct changes in the B, C, and Na K-edges spectra can be identified. The spectra collected for NCB milled for <1 h, i.e., 15, 30, and 45 min, are similar to the pristine NCB, hence they are not shown in the figure. Interestingly, in this range of milling time (0–60 min), despite the structural variations in which the NCB undergoes a phase transformation from orthorhombic to cubic (bcc) leading to increased ionic conductivity,[24] no particular local electronic modifications are evidenced around the scatterer. On the other hand, a milling

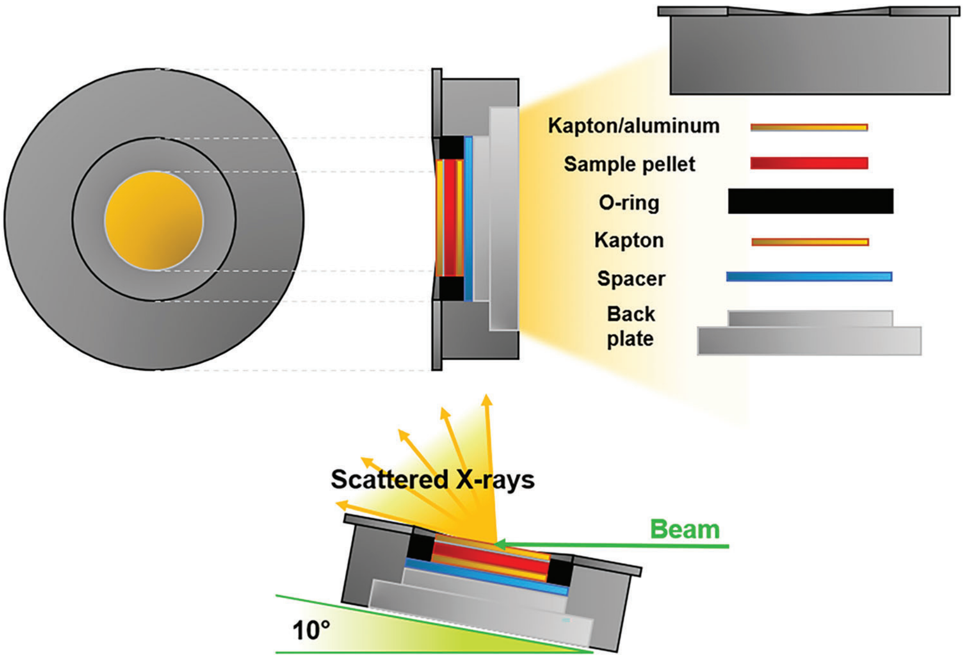

Figure 1. Schematic representation of the air-tight custom-made cell used for XRS measurements.

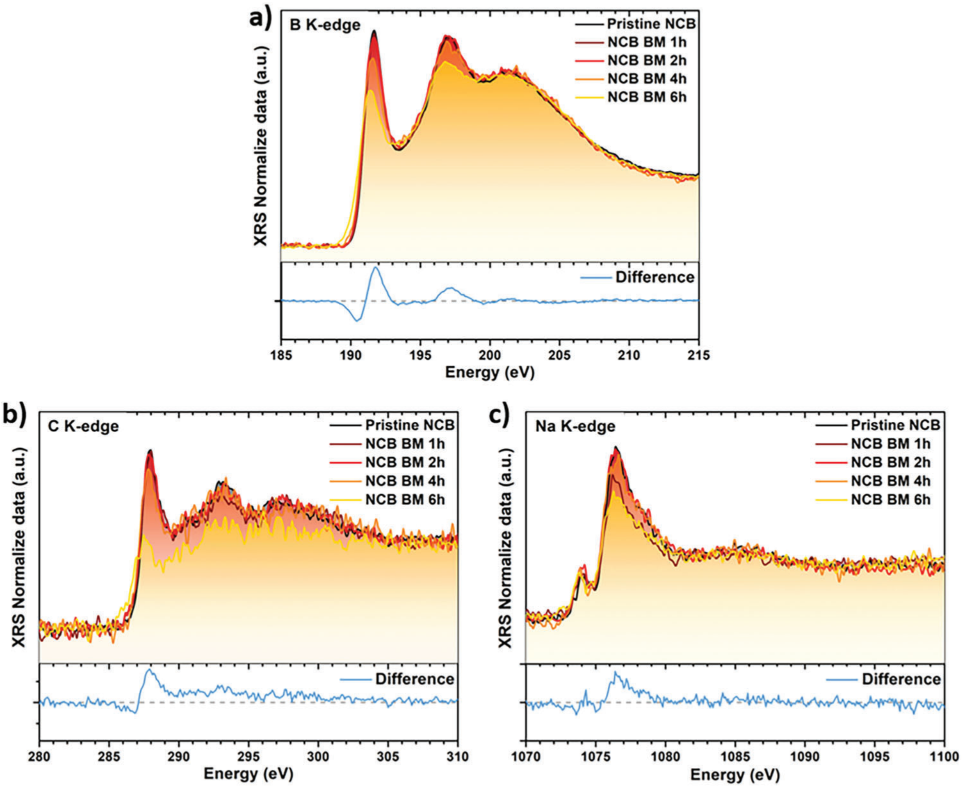

Figure 2. a) B K-edge, b) C K-edge, and c) Na K-edge XRS spectra of pristine NCB and a function of milling time. The difference has been calculated between the pristine and 6 h milled NCB spectra. The dashed grey line corresponds to 0.

treatment longer than 1 h affects the electronic structure of the B, C, and Na of the NCB. The main differences as a function of the milling time in Figure 2, highlighted on the bottom of the spectra as a difference between the spectra collected from the pristine and 6 h milled NCB, correspond to the decrease intensity of the first and second peaks in the B and C K-edge spectra and the decrease of the second peak in the Na K-edge.

To gain insight into the effects of long-term mechanical milling, XRS spectra were compared to selected reference compounds (see Figure S1, Supporting Information). However, the comparison with reference compounds could not explain the changes observed in the spectra of the milled samples. This is not unexpected because the main change in the spectra is the reduced intensity of the peaks associated with the different transitions described above. Unexpectedly, the B and Na K-edge spectra of $Na_2B_{12}H_{12}$ are quite similar to those of the pristine $NaCB_{11}H_{12}$ indicating that the presence of carbon in the boron cage ($CB_{11}H_{12}^-$), and the reduced charge of the complex anion, does not have a significant effect on the electronic structure of the boron and sodium atoms. As expected, the spectra of $NaBH_4$ and $B_{10}H_{14}$ reference compounds were found to be clearly different from those of NCB.

To explore the electronic structure of the NCB as a function of the milling time, B, C, and Na K-edge DFT simulations were performed using the Finite Difference Method Near Edge Structure (FDMNES) software package.[38] The B, C, and Na electronic structure calculations have been performed using the orthorhombic ($Pca2_1$) structure of the $NaCB_{11}H_{12}$, as a starting structural model, and by using two semi-empirical parameters, i.e., screening and dilatorb (0<screening/dilatorb<1).[38–41] The degree of covalency in a material can be adjusted by modifying certain parameters. One of those parameters is dilatorb, which alters the spatial extent of the valence orbitals. A high dilatorb value leads to greater covalency, as it enhances the overlap between the absorber and first neighbor orbitals. Dilatorb is particularly useful for simulating atoms in an ionic state, and it can be adopted for any ionic species. Another parameter is the screening parameter, which modifies the electronic charge in a partially occupied valence orbital of the absorber. In a self-consistent calculation, neighboring atoms can participate in the core-hole screening by transferring electrons to or from the absorber. This parameter helps to simulate the interaction between the absorber and its neighbors by artificially adding extra screening charges from them. In this work, screening refers to the interaction between a B atom and its environment. The screening value, which is applied to the absorber atoms, increases the negative charge on the absorbing atom and decreases the interaction and electron transfer with its environment.

The simulations in the next section were performed following different steps: first, using input configurations based on the structure obtained through XRD analysis, especially to optimize the values of the semi-empirical parameters, and second, considering $NaCB_{11}H_{12}$ as a single molecule. In both cases, we considered the impact of the dilatorb and screening parameters.

2.2. Simulations Using Crystallographic Input

DFT calculations with FDMNES, which involve the use of two semi-empirical parameters, to model the electronic structure of the studied systems, have been performed. The results of these calculations and the impact of the chosen parameters on the calculated signals are presented in Figures S2–S4 (Supporting Information) for the B, C, and Na K-edges, respectively.

In **Figure 3**, the calculated spectra obtained using a combination of parameters that best match the experimentally obtained spectra (in terms of both peak position and relative intensities), are reported. For the B and C K-edges, this combination was a screening parameter of 0.5 and a dilatorb parameter of 0, while for the Na K-edge, a screening parameter of 1 and a dilatorb parameter of 0 provided the best match. The calculated spectra obtained using these parameters are in appreciable agreement with the experimental data, considering the lack of robust models and programs for simulating XRS spectra. This indicates that the chosen parameters provide a reliable approximation of the electronic structure of the systems being studied.

A possible explanation of the effect reported in Figure 3a, Figures S2 and S5 (Supporting Information) and related to the use of screening parameters, can be attributed to the benzene-like behavior, i.e., 3D delocalization of the electrons which have been reported for the closo-borates anions.[42,43] The screening parameter equal to 0.5 considers the electronic correlation occurring on the B atom due to the strong interaction with its local environment. Hence, this parameter is crucial for a satisfactory agreement between the experimental and the calculated spectra.

For the B K-edge (Figure 3a and Figure S2, Supporting Information), an increase in the screening parameter from 1 to 0.1 resulted in several changes in the spectrum: I) the first and second peaks shifted to higher energy; II) the third peak shifted to lower energy; III) the first peak decreased in intensity; IV) the second peak increased in intensity. The best agreement between the experimental and calculated spectra was achieved when the screening parameter was set to 0.5, especially in terms of the relative intensity of the first and second peaks.

Considering the C K-edge, all the calculated spectra show a pre-edge that is not present in the experimental signals (Figure S3, Supporting Information). The dilatorb parameter, also in this case has a minor impact on the calculated spectra (see supporting information). On the other hand, increasing the screening parameter (as shown in Figure S3, Supporting Information) allows us to observe that: I) the pre-edge shift to higher energy; II) the first peak shift to higher energy and increases in intensity; III) the second peak does not shift, but decreases in intensity. In contrast to the experimental signal, the calculated spectrum does not show a third feature/peak at high energy (≈12 eV). As for the B K-edge results, the best agreement between the experimental and calculated spectra, which is mainly based on the matching of the relative intensities of the first and second peaks with the experimental signals, is obtained when the screening parameter is set to 0.5 (Figure 3b). The same optimal screening parameter, i.e., 0.5, for the boron and the carbon, is expected since both the boron and carbon are in the aromatic-like $CB_{11}H_{12}$ cage, sharing the same delocalization of electrons.

Finally, considering the Na K-edge shown in Figure S4 (Supporting Information), it can be highlighted that: I) the pre-edge shifts to lower energy and doubles; II) the pre-edge increases in intensity; III) the first peak shifts to higher energy. The best agreement between the experimental and the calculated spectra is obtained when the screening parameter is equal to 1.0 and dilatorb

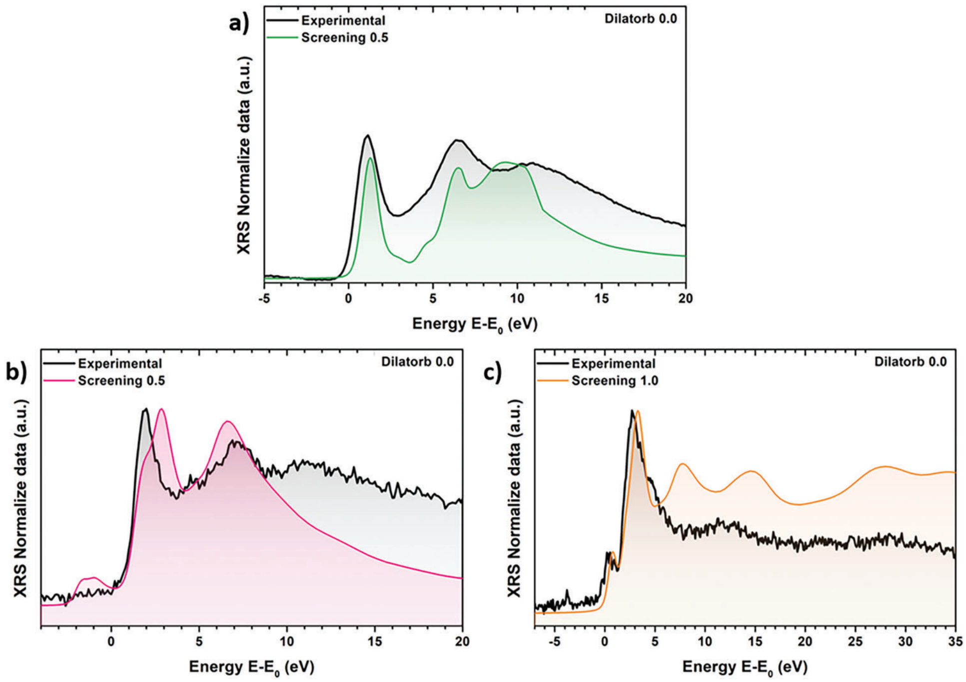

Figure 3. Simulated a) Boron, b) Carbon, and c) Sodium K-edge spectra using the screening parameter equal to a) 0.5, b) 0.5, and c) 1.0 and the dilatorb parameter equal to 0.

equal to 0, which suggests no screening effect (Figure 3c). This suggests that the electronic configuration of the sodium is not affected by the $CB_{11}H_{12}$ cage. This observation is not surprising since the Na^+ and $CB_{11}H_{12}^-$ are ionically bonded, therefore any shared electrons are partially delocalized.

From these simulations, we have been able to define the optimized semi-empirical parameters (dilatorb and screening) to be used for the following analysis.

2.3. Simulations Using a $NaCB_{11}H_{12}$ Molecule as input

The agreement between the calculated and experimental spectra confirms the reliability of the measurement procedure, cells, and the methods used to perform the DFT calculations. Although the information extracted from the calculations is of interest from a fundamental point of view, as it confirms the aromaticity of $CB_{11}H_{12}^-$ and its ionic interaction with Na^+, we could not fully explain the changes in the B, C, and Na K-edges at long milling times, as highlighted in Figure 2. To address this, we used a different approach compared to the one discussed thus far. In this case, only the ideal molecule of $NaCB_{11}H_{12}$ was considered as input. This approach allowed us to evaluate the different contributions of the B atoms in the calculated signal by considering as input a $NaCB_{11}H_{12}$ molecule. Accordingly, the position of the Na^+ relative to the position of the carbon in the $CB_{11}H_{12}^-$ cage was determined based on calculations performed by Dimitrievska et al.[13] Specifically, the vector to the C atom and the vector to the Na^+ were found to form an angle of 142.8°, and the Na^+ was found to be bound to the face of the icosahedron farthest from the carbon axis (see **Figure 4**b). Instead of calculating the average B-edge of the molecule, each of the 11 different B atoms of the molecule was simulated separately, as highlighted in different colors in Figure 4a. The calculation has been performed with a dilatorb parameter equal to 0.0 and a screening parameter of either 0.5 or 0.0 (Figure 4a and Figure S5, Supporting Information, respectively), which goes along with the best agreement obtained in Figure 3. The results of the B-edge calculation are reported in Figure 4a, and the distance between the Na^+ and each boron atom in the $CB_{11}H_{12}^-$ cage is shown in Figure 4c. The calculated C and Na K-edges resulting from this approach are shown in Figure S6 (Supporting Information).

Importantly, the calculated B-edge spectra according to this approach (Figure 4b) have allowed us to highlight clearly the drastic electronic changes for the B atoms that are in the proximity of the Na^+. The calculated spectra of the boron atoms closer to the Na^+, i.e., B8, B9, and B11 (B atoms forming the icosahedral that faces the Na^+), show that compared to the experimental obtained spectra, I) the first peak is completely depressed and II) the intensity of the second peak is enhanced, due to the presence of the Na^+ which shares its electron, contributing to a partial occupying the antibonding π^* ($2a_1$) orbital.

All the other spectra show a different relative intensity between the first and the second peak, with the first peak much more intense. In addition, the first peak is doubled for the boron (B_1, B_2, $B_{5,}$ and B_6) atoms that are close to the carbon.

While Figure 4 can explain the results at long milling times in the B K-edge (Figure 2a), it cannot explain the drastic differences in the C K-edge (Figure 2b). Therefore, an additional DFT calculation was performed. In this case, the ideal molecule of $NaCB_{11}H_{12}$ was considered as input, and the C K-edge was calculated (**Figure 5**a) for each of the 12 possible positions in the $CB_{11}H_{12}$ cage (Figure 5b). Figure 5a shows the results obtained from the C K-edge calculation in all 12 possible positions (where

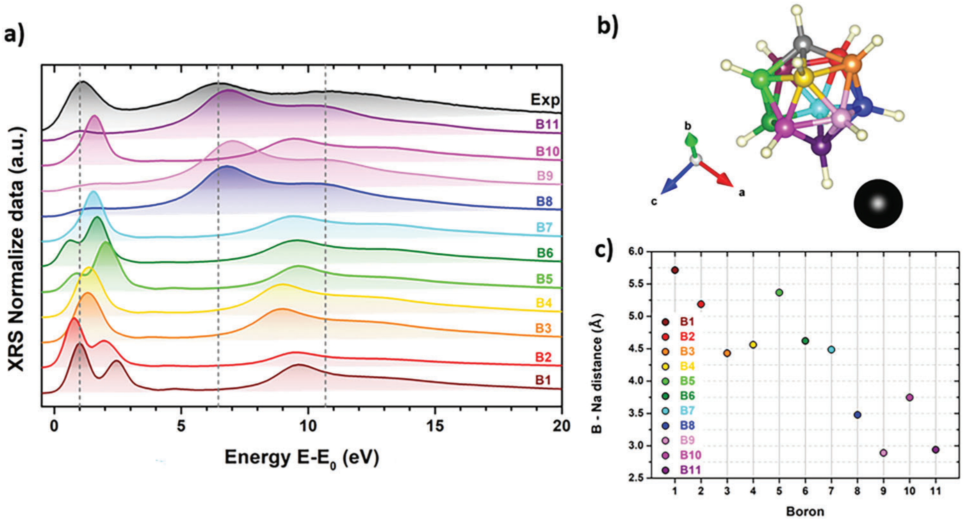

Figure 4. a) The simulated boron K-edge spectra (screening parameter 0.5) of each boron of the CB11H12− cage. The spectra collected experimentally for the pristine NCB (black solid line) are also reported. b) Structure of the molecule used as input for the ab initio calculation where each boron is highlighted with a different color, while the Na is highlighted in black and the carbon in grey. c) B-Na distance for each boron in the CB11H12− cage. The Fermi level is slightly shifted for all the different B atoms according to their different surroundings.

C_0 is the stable position in the $CB_{11}H_{12}$ cage), while Figure 5c shows the distance between the Na^+ and each carbon position. The calculation was performed with a dilatorb parameter equal to 0.0 and a screening parameter of 0.5, by Figure 3b.

The output of this calculation is of crucial importance since it demonstrates how the C—Na distances are intimately related to the C K-edge spectra. The calculated spectra showed that when the carbon is located on the icosahedral face facing the sodium ions (C_8, $C_{9,}$ and C_{11}), the first peak is completely depressed and the intensity of the second peak is enhanced due to the partial filling of the state resulting from the electron contribution of the sodium ions. These results are comparable to those reported in Figure 4.

3. Discussion

Figure 2a,b shows that when the milling time exceeds 1 h, the intensity of the first and the second peaks decreases, even though

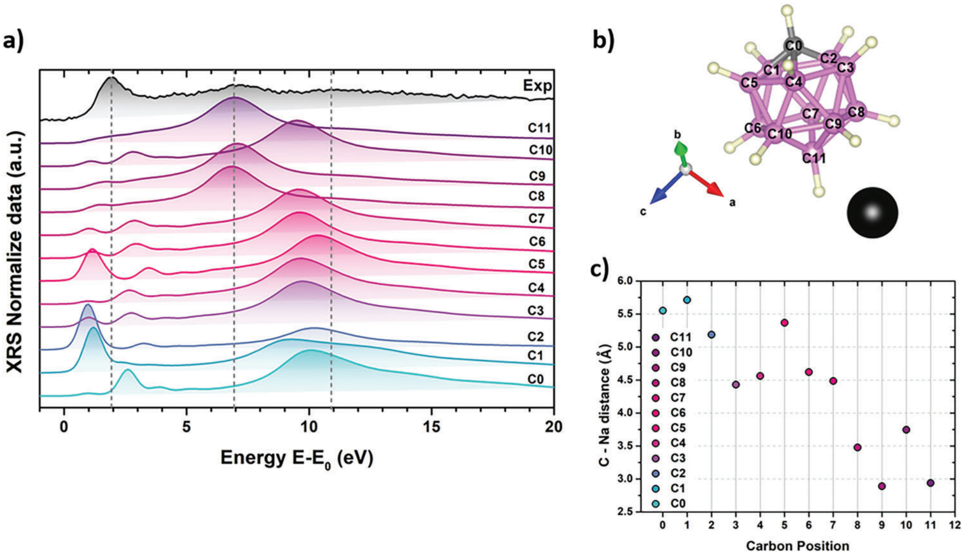

Figure 5. a) The simulated carbon K-edge spectra (screening parameter 0.5) in each possible position (12) of the $CB_{11}H_{12}^-$ cage. The spectra collected experimentally for the pristine NCB (black solid line) are also reported. b) Structure of the molecule used as input for the ab initio calculation where each position is highlighted with a different number, Na is highlighted in black and the carbon stable position (C0) in grey. c) C-Na distance for each position possible in the $CB_{11}H_{12}^-$ cage. The Fermi level is slightly shifted for all the different B atoms according to their different surroundings.

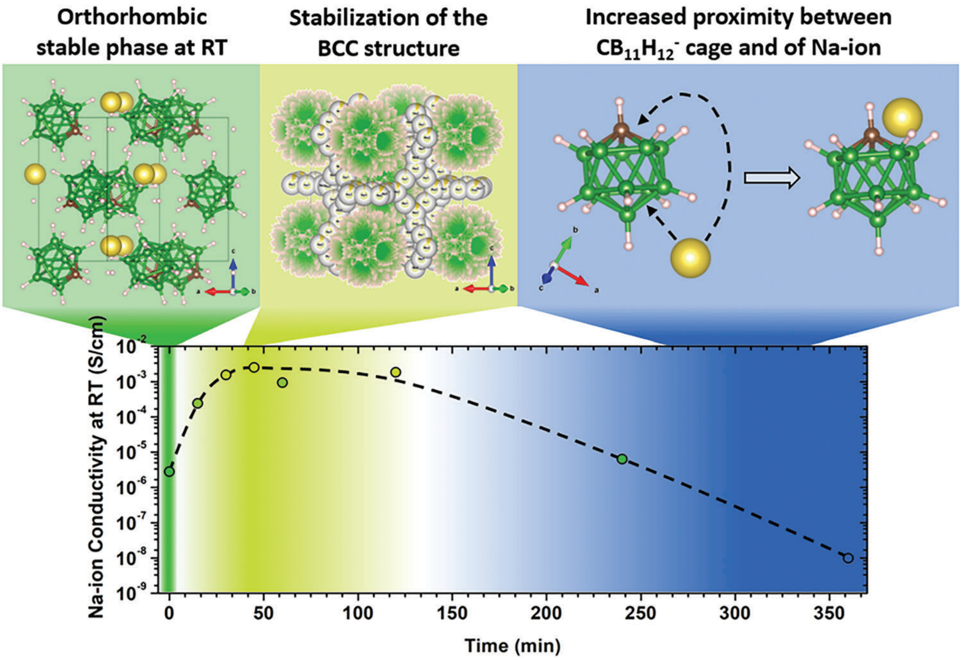

Figure 6. Na-ion conductivity as a function of the milling time, together with this work concluded a possible structural effect. The dashes line is a guide for the eyes. Adapted with permission.[24] Copyright 2021, American Chemical Society.

with a different ratio (stronger effect on the first peak). In addition, a mechanical treatment longer than 2 h decreases drastically the conductivity of NCB (**Figure 6**).

Based on the computed spectra (Figures 4 and 5) it is clear that the crystallographic long-range structure (from XRD) and the element-specific short-range structure (from XRS) are obviously not identical, even though they both describe structural aspects that are certainly related. Such difference has been observed in some systems and was ascribed to defects/disorders, and/or secondary phases in the original structure, arising from doping, alloying, or even mechanical milling.[44] Upon 45 min milling, XRD results show that the degree of crystallinity decreases (see Figure S7, Supporting Information),[24] and further milling to >2 h leads to an almost amorphous structure. The increased Na-ion conductivity upon milling for 45 min has been related to the stabilization of the bcc polymorph at RT,[24] that should be electronically identical. This is in line with the XRS results, which show that the difference between the pristine structure and the milled one arises only after 1 h of milling. We explain this as a consequence of high defects/vacancies or distortion of the NCB structure due to the mechanical milling. Based on the results of the XRS simulations from the B K-edge, the significant decrease in intensity of the first peak at milling times higher than 2 h can be attributed to a closer proximity of the Na^+ to the $CB_{11}H_{12}$ (Figure 5) arising from the mechanical distortion of the structure during milling. This is highlighted in the XRS results as a reduction of the first peak in both B, C, and Na K-edges. This also follows earlier results where it has been shown that the relative intensities of the two main peaks in the Na K-edge spectra are a reasonable indicator of the Na coordination environment, the more disordered the Na environment, the broader the peaks.[45] In addition, the intensity of the first peak tends to decrease relative to the second peak when the Na coordination increases, in line with our results (Figures 2,5, and 6).[45] Therefore we conclude that the higher degree of structural distortion in the over-milled NCB is the origin of the decrease in the Na ion conductivity.

A similar mechanochemically induced decrease in ionic conductivity was reported recently for the thiophosphate $Li_{10}GeP_2S_{12}$ (LGPS).[46] The authors showed that the bulk ionic conductivity of the LGPS decreased by a factor of 10 when milled for 2 h. Using XRD, NMR measurements, and broadband conductivity spectroscopy in combination with electric modulus measurements, they related this effect to structural heterogeneity introduced in the samples by the ball milling process, i.e., formation of nanocrystallites LGPS next to structurally amorphous regions of LGPS. The very low conductivity of the amorphous (high-defected) regions, compared to the crystalline fraction, leads to a profound decrease in the overall conductivity of the ball-milled samples. It was concluded that, unlike solid electrolytes with poor ionic conductivity, the introduction of higher dimensional structural disorder in originally highly conducting solid electrolytes with crystallographically well-defined ion diffusion pathways, lowers the conductivity. Thus, such disorders hinder long-range ion transport through the crystal structure.

As no distinct secondary phase can be detected in our samples (neither with NMR nor DRIFTs),[24] which could have led to the lowering of the overall conductivity, we attribute the decrease in ionic conductivity mostly to the decrease in the distance between Na^+ and $CB_{11}H_{12}$ cage due to the severe structural distortion of the NCB structure during ball milling. Such close proximity can result in a stronger electrostatic interaction between the $CB_{11}H_{12}^-$ and the Na^+ and consequently lower Na-ion conductivity. It has also been shown that a vacancy concentration above 50% is generally detrimental to fast ion mobility in solid electrolytes.[47] Therefore, we can conclude that the bulk NCB (non-ball milled) possesses some defects based on the difference between the proposed crystalline structure and the element-specific structure from the computation. Ball milling for 1 h or less leads to stabilizing a different polymorph, thereby increasing the ion conductivity. However, extended milling times lead to severe structural distortion and/or higher vacancy concentrations which is detrimental to the long-range ion transport/diffusion. These results highlight the complex interplay between the structural defects/vacancy concentrations and ion dynamics and that an accurate understanding of this relationship is pivotal for the development of novel solid electrolytes with high ionic conductivities.

4. Conclusion

In this study, we used X-ray Raman Scattering Spectroscopy to investigate the impact of mechanochemical treatment on the structure and ionic conductivity of $NaCB_{11}H_{12}$. For the first time, the B, C, and Na K-edges of this material were successfully measured, and we observed similarities in spectra for milling times not higher than 1 h, with differences becoming apparent for samples milled for 4 and 6 hours. Ab initio calculations combined with the use of semi-empirical parameters allowed computation and interpretation of the XRS spectra. A clear difference is observed between the measured spectra and the expected spectra based on the reported crystallographic structure, showing that the element-specific electronic structure is different. The use of screening parameters enabled us to unravel that this is due to the aromatic-like behavior of the $CB_{11}H_{12}$ cage, hence delocalized electrons. Considering $NaCB_{11}H_{12}$ as a molecule instead of the crystallographic structure, enabled the computation of element-specific structure, representing all the possible distances between the elements (B—Na and C—Na). Using this approach, a closer proximity, arising from the mechanical distortion of the structure during milling, between the Na^+ and the $CB_{11}H_{12}$ has been highlighted. This strongly suggests that severe structural distortion of the NCB upon prolonged mechanical milling, is the cause of the decreased Na-ion conductivity. These results underline the intricate interplay between structure and ion dynamics, hence accurate understanding of this relationship is crucial for the development of solid electrolytes with excellent conductivity. Our work also highlights the unique potential of XRS for studying the structural and electronic changes in a variety of lightweight solid electrolytes, especially the complex hydrides that typically contain low Z elements such as Li, B, C, Na, and N.

5. Experimental Section

$NaCB_{11}H_{12}$ (NCB) was purchased from KatChem and it was dried at 180 °C under a dynamic vacuum for 12 h. Subsequently, it was milled in an 8000 M Mixer-Mill (Spex) for selected milling times, ranging from 15 min to 6 h, using a stainless-steel jar with ball-to-powder weight ratio of 1:180, following the reported synthesis by Murgia et al..[24] The compounds ($Na_2B_{12}H_{12}$, KatChem, $NaBH_4$ Sigma–Aldrich, 99.99 %, and $B_{10}H_{14}$) used as a reference for the XRS results, were purchased and used without further modifications.

Sodium (Na), boron (B), and carbon (C) K-edge XRS spectra were collected at both ESRF ID20 and DESY Petra III P01. Specifically, the boron K-edge spectra and the reference samples were measured at ID20 ESRF, while the NCB samples were measured at Petra III P01. An air-tight, custom-made cell was mounted on a pre-constructed cell holder in an incidence configuration with a 10° angle to the beam. The sample preparation consists of compression of ≈10–40 mg of sample to form a 10 mm diameter pellet, using a hydraulic press (250 MPa). The pellet was then placed in the XRS cell in between a Kapton foil and a Kapton/aluminum foil (incident beam side). All storage and handling of the chemicals was done in an argon-filled glovebox (H_2O and $O_2 < 0.1$ ppm). The incident photon energy was set using a Si(311) monochromator. The XRS scans were performed using the inverse energy scan technique, in which the scattered photons were analyzed at a fixed energy and the energy transfer was controlled by tuning the incident photon energy. The XRS spectra were collected by scanning the incident beam energy relative to the fixed analyzer energy of 9690 eV with a resolution of 0.7 eV. The XRS spectra were collected using Medipix detectors (2D photon-counting X-ray detectors with a 55 µm spatial resolution)[48] with an average q-vector of 4.5 inverse Å ($2\theta = 55°$). The data were treated with the XRStools program package as described elsewhere.[49,50] To elucidate the electronic structure of the materials, B, Na, and C K-edge ab initio simulations were performed using the Finite Difference Method Near Edge Structure (FDMNES) software package.[39]

Supporting Information

Supporting Information is available from the Wiley Online Library or from the author.

Acknowledgements

Financial support from The Netherlands Organization for Scientific Research (NWO-ECHO and NWO-RELEASE) was gratefully acknowledged. The authors kindly acknowledge Marcel Van Asselen and Sander Deelen for the design of the cell, and Masoud Lazemi for the support in the laboratory activities, all from Utrecht University. We acknowledge the European Synchrotron Radiation Facility (ESRF) for provision of synchrotron radiation facilities under proposal number CH-6019 as well as computing resources and we would like to thank F. Gerbon for assistance and support in using beamline ID20. Part of the research presented in this document was carried out at PETRA III synchrotron (DESY) beamline P01, Hamburg, Germany.

Conflict of Interest

The author declares no conflicts of interest.

Data Availability Statement

The data that support the findings of this study are available from the corresponding author upon reasonable request.

Keywords

all-solid-state batteries, complex hydrides electrolytes, closo-carbadodecaborate, solid-state electrolytes, sodium-ion conductors, X-ray Raman scattering (XRS)

Received: July 4, 2023
Revised: September 4, 2023

[1] S. Ferrari, M. Falco, A. B. Muñoz-García, M. Bonomo, S. Brutti, M. Pavone, C. Gerbaldi, *Adv. Energy Mater.* **2021**, 11.
[2] I. Hasa, S. Mariyappan, D. Saurel, P. Adelhelm, A. Y. Koposov, C. Masquelier, L. Croguennec, M. Casas-Cabanas, *J. Power Sources* **2021**, *482*, 228872.
[3] F. Cuevas, M. B. Amdisen, M. Baricco, C. E. Buckley, Y. W. Cho, P. de Jongh, L. M. de Kort, J. B. Grinderslev, V. Gulino, B. C. Hauback, M. Heere, T. Humphries, T. R. Jensen, S. Kim, K. Kisu, Y.-S. Lee, H.-W. Li, R. Mohtadi, K. T. Møller, P. Ngene, D. Noréus, S. Orimo, M. Paskevicius, M. Polanski, S. Sartori, L. N. Skov, M. H. Sørby, B. C. Wood, V. A. Yartys, M. Zhu, et al., *Prog. Energy* **2022**, *4*, 032001.
[4] R. Cerný, F. Murgia, M. Brighi, *J. Alloys Compd.* **2022**, *895*, 162659.
[5] L. Duchêne, A. Remhof, H. Hagemann, C. Battaglia, *Energy Storage Mater.* **2019**.
[6] R. Asakura, D. Reber, L. Duchêne, S. Payandeh, A. Remhof, H. Hagemann, C. Battaglia, *Energy Environ. Sci.* **2020**, *13*, 5048.
[7] R. Asakura, L. Duchêne, S. Payandeh, D. Rentsch, H. Hagemann, C. Battaglia, A. Remhof, *ACS Appl. Mater. Interfaces* **2021**.
[8] R. Asakura, L. Duchêne, R.-S. Kühnel, A. Remhof, H. Hagemann, C. Battaglia, *ACS Appl. Energy Mater.* **2019**, *2*, 6924.
[9] R. Černý, M. Brighi, F. Murgia, *Chemistry (Easton)*. **2020**, *2*, 805.
[10] R. N. Grimes, in *Carboranes* (Eds.: R. J. Binder, P. K. Srivastava), Elsevier, Cham **2016**, pp. 1–5.
[11] M. Brighi, F. Murgia, Z. Lodziana, P. Schouwink, A. Wolczyk, R. Cerny, *J. Power Sources* **2018**, *404*, 7.
[12] S. Kim, H. Oguchi, N. Toyama, T. Sato, S. Takagi, T. Otomo, D. Arunkumar, N. Kuwata, J. Kawamura, S.-I. Orimo, *Nat. Commun.* **2019**, *10*, 1081.
[13] M. Dimitrievska, P. Shea, K. E. Kweon, M. Bercx, J. B. Varley, W. S.i Tang, A. V. Skripov, V. Stavila, T. J. Udovic, B. C. Wood, *Adv. Energy Mater.* **2018**, *8*, 1703422.
[14] N. Verdal, T. J. Udovic, V. Stavila, W. S.i Tang, J. J. Rush, A. V. Skripov, *J. Phys. Chem. C* **2014**, *118*, 17483.
[15] A. V. Soloninin, R. V. Skoryunov, O. A. Babanova, A. V. Skripov, M. Dimitrievska, T. J. Udovic, *J. Alloys Compd.* **2019**, *800*, 247.
[16] S. Kim, N. Toyama, H. Oguchi, T. Sato, S. Takagi, T. Ikeshoji, S.-I. Orimo, *Chem. Mater.* **2018**, *30*, 386.
[17] M. Brighi, F. Murgia, R. Cerný, *Cell Reports Phys. Sci.* **2020**, *1*, 100217.
[18] F. Murgia, M. Brighi, R. Cerný, *Electrochem. Commun.* **2019**, *106*, 106534.
[19] L. M. De Kort, O. E. Brandt Corstius, V. Gulino, A. Gurinov, M. Baldus, P. Ngene, *Adv. Funct. Mater.* **2023**, *33*, 2209122.
[20] L. M. De Kort, V. Gulino, P. E. De Jongh, P. Ngene, *J. Alloys Compd.* **2022**, *901*, 163474.
[21] L. De Kort, P. Ngene, M. Baricco, P. De Jongh, V. Gulino, *J. Phys. Chem. C* **2023**, *127*, 3988.
[22] S. A. Humphry-Baker, S. Garroni, F. Delogu, C. A. Schuh, *Nat. Mater.* **2016**, *15*, 1280.
[23] J. A. Dawson, M. S. Islam, *ACS Mater. Lett.* **2022**, *4*, 424.
[24] F. Murgia, M. Brighi, L. Piveteau, C. E. Avalos, V. Gulino, M. C. Nierstenhöfer, P. Ngene, P. De Jongh, R. Cerný, *ACS Appl. Mater. Interfaces* **2021**, *13*, 61346.
[25] W. S.i Tang, A. Unemoto, W. Zhou, V. Stavila, M. Matsuo, H. Wu, S.-I. Orimo, T. J. Udovic, *Energy Environ. Sci.* **2015**, *8*, 3637.
[26] P. S. Miedema, in *Raman Spectroscopy and Applications*, InTech, **2017**.
[27] P. S. Miedema, P. Ngene, A.d M. J. Van Der Eerden, T.-C. Weng, D. Nordlund, D. Sokaras, R. Alonso-Mori, A. Juhin, P. E. De Jongh, F. M. F. De Groot, *Phys. Chem. Chem. Phys.* **2012**, *14*, 5581.
[28] P. S. Miedema, P. Ngene, A.d M. J. Van Der Eerden, D. Sokaras, T.-C. Weng, D. Nordlund, Y. S. Au, F. M. F. De Groot, *Phys. Chem. Chem. Phys.* **2014**, *16*, 22651.
[29] C. J. Sahle, S. Kujawski, A. Remhof, Y. Yan, N. P. Stadie, A. Al-Zein, M. Tolan, S. Huotari, M. Krisch, C. Sternemann, *Phys. Chem. Chem. Phys.* **2016**, *18*, 5397.
[30] A. Rajh, I. Arcon, K. Bucar, M. Zitnik, M. Petric, A. Vizintin, J. Bitenc, U. Kosir, R. Dominko, H. Gretarsson, M. Sundermann, M. Kavcic, *J. Phys. Chem. C* **2022**, *126*, 5435.
[31] M. Fehse, C. J. Sahle, M. P. Hogan, C. Cavallari, E. M. Kelder, M. Alfredsson, A. Longo, *J. Phys. Chem. C* **2019**, *123*, 24396.
[32] T. Nonaka, H. Kawaura, Y. Makimura, Y. F. Nishimura, K. Dohmae, *J. Power Sources* **2019**, *419*, 203.
[33] S. Huotari, T. Pylkkänen, R. Verbeni, G. Monaco, K. Hämäläinen, *Nat. Mater.* **2011**, *10*, 489.
[34] P. Tack, E. De Pauw, B. Tkalcec, A. Longo, C. J. Sahle, F. Brenker, L. Vincze, *Anal. Chem.* **2021**, *93*, 14651.
[35] R. Georgiou, P. Gueriau, C. J. Sahle, S. Bernard, A. Mirone, R. Garrouste, U. Bergmann, J.-P. Rueff, L. Bertrand, *Sci. Adv.* **2019**, *5*, 1.
[36] S. K. Lee, P. J. Eng, H.-K. Mao, *Rev. Mineral. Geochemistry* **2014**, *78*, 139.
[37] P. Skytt, P. Glans, D. C. Mancini, J.-H. Guo, N. Wassdahl, J. Nordgren, Y. Ma, *Phys. Rev. B* **1994**, *50*, 10457.
[38] Y. Joly, C. Cavallari, S. A. Guda, C. J. Sahle, *J. Chem. Theory Comput.* **2017**, *13*, 2172.
[39] C. Chen, D. Chen, Y. Gao, Z. Shao, F. Ciucci, *J. Mater. Chem. A* **2014**, *2*, 14154.
[40] R. Wernert, L. H. B. Nguyen, E. Petit, P. S. Camacho, A. Iadecola, A. Longo, F. Fauth, L. Stievano, L. Monconduit, D. Carlier, L. Croguennec, *Chem. Mater.* **2022**.
[41] G. Raimondi, A. Longo, F. Giannici, R. Merkle, M. F. Hoedl, A. Chiara, C. J. Sahle, J. Maier, *J. Mater. Chem. A* **2022**, *10*, 8866.
[42] P. V. R. Schleyer, K. Najafian, *Inorg. Chem.* **1998**, *37*, 3454.
[43] J. Aihara, *J. Am. Chem. Soc.* **1978**, *100*, 3339.
[44] E. Haubold, P. Schöppe, S. Eckner, S. Lehmann, I. Colantoni, F. D'acapito, F. Di Benedetto, S. Schorr, C. S. Schnohr, *J. Alloys Compd.* **2019**, *774*, 803.
[45] G. S. Henderson, F. M. F. De Groot, B. J. A. Moulton, *Rev. Mineral. Geochemistry* **2014**, *78*, 75.
[46] L. Schweiger, K. Hogrefe, B. Gadermaier, J. L. M. Rupp, H. M. R. Wilkening, *J. Am. Chem. Soc.* **2022**, *144*, 9597.
[47] J. B. Goodenough, *Proc. R. Soc. A Math. Phys. Eng. Sci.* **1984**, *393*, 215.
[48] Ponchut, Cyril, J. Clément, J-M. Rigal, E. Papillon, J. Vallerga, D. LaMarra, B. Mikulec, Nuclear Instruments and Methods in Physics Research Section A: Accelerators, Spectrometers, Detectors and Associated Equipment **2007**, *576*, 109.
[49] D. L. Johnson, *Phys. Rev. B* **1974**, *9*, 4475.
[50] C.h. J. Sahle, A. Mirone, J. Niskanen, J. Inkinen, M. Krisch, S. Huotari, *J. Synchrotron Radiat.* **2015**, *22*, 400.